CRUSTAL DEFORMATION OF THE SAN ANDREAS FAULT SYSTEM

A FINAL REPORT SUBMITTED TO THE DEPARTMENT OF EARTH SCIENCES, UNIVERSITY OF HAWAI'I AT MĀNOA, IN PARTIAL FULFILLMENT OF THE REQUIREMENTS FOR THE DEGREE OF

MASTER OF SCIENCE
IN
EARTH AND PLANETARY SCIENCES

OCTOBER 2019
BY
LAUREN WARD

COMMITTEE:
BRIDGET SMITH-KONTER (CHAIR)
JAMES FOSTER
PAUL WESSEL

Abstract

The San Andreas Fault System (SAFS) has the potential to cause unprecedented economic and infrastructure damages, as well as human loss, among the millions of people who live in the region. To improve the current understanding of this dynamic fault system, the goal of this work is to advance methods to study and quantify the region's seismic hazards. To achieve this goal, an accurate representation of the SAFS through modeling the earthquake cycle and integration of geodetic data is critical. The SAFS covers hundreds of kilometers throughout California, crossing multiple geologic boundaries, thus including additional fault-specific characteristics enhance the confidence had for the model as it creates a more realistic representation of the fault system. Furthermore, existing models generally prescribe average values for fault parameters such as an average crustal rigidity of 30 GPa. Unique to this study is the consideration of variable crustal rigidity and the deformation changes that may result. When assessing modeled surface deformation, it was found that for regions prescribed a value of 50% lower than average crustal rigidity, the deformation rate increased by at least 66%. In contrast, regions of 50% higher than average crustal rigidity had a decreased deformation rate by at least 61%. The modeled rates of deformation can be further applied to calculate seismic moment accumulation rates which provide information about the current level of strain of the system and in turn its seismic risk.

A supplemental analysis of available geodetic data (GPS and InSAR combinations) was also performed for this investigation to ensure quality data selection and weighting. Results from this analysis suggest that the Southern California Earthquake Center (SCEC) Community Geodetic Model (CGM) GPS data set and the ALOS InSAR data set yield the lowest weighted root mean square velocity residual and thus were used for analysis. When utilizing these geodetic data and inverting for fault slip rate for both a homogenous average crustal rigidity model and a variable crustal rigidity model of the SAFS, significant differences are observed. Specifically, for the more

inclusive variable crustal rigidity model, regions such as the Salton Trough, with a lower than average crustal rigidity, results in a decreased seismic moment rate (0-4 Nm/km/100 years) as opposed to the previous estimates assuming a homogeneous model (0-17 Nm/km/100 years).

Table of Contents

1 Introduction

The vast SAFS extends nearly 1,200 kilometers through California, intersecting major and heavily populated cities, including Los Angeles, San Diego and San Francisco, and is home to over 10 million people (Field et al., 2015). The SAFS is well-known as the major tectonic plate boundary that pushes the Pacific Plate northwest and the North American Plate southeast. The SAFS however, is much more complicated than a single plate boundary and is comprised of a complex network of over 40 fault segments (Figure 1). The complicated nature of the fault system subjects the region and population to high seismic risk caused by variations in the earthquake cycle as multiple moderate to major earthquakes have occurred there over the past 200 years (Smith and Sandwell, 2006). During an earthquake cycle, interseismic strain is accumulated from applied forces due to tectonic plate movement. This strain is then released through coseismic slip from a seismic event and afterwards, postseismic viscoelastic relaxation may occur within the uppermost layers of the Earth. Previous studies demonstrate that while earthquakes do not always adhere to specific cyclic patterns (Weldon et al., 2004), quantifying interseismic strain accumulation provides critical information about where a fault may be in the earthquake cycle. Another important quantity, the seismic moment accumulation rate (Equation 1) determined by slip rate (s) and area of the fault (A), and elastic properties of the Earth's crust (crustal rigidity, μ) (Kostrov 1974), is the rate at which the fault accumulates seismic moment for a subsequent event:

$$M_o = \mu s A \qquad (1)$$

As seismic moment of an earthquake is a measure of the magnitude of a seismic event, it thus relates the potential of a fault to its seismic hazard (Stein, 2007). For the SAFS, one example of a region scientists are particularly concerned about is in the southern section near Coachella (COA), which has not had a major earthquake in the past three centuries (Williams et al., 2010). This absence of moment release has thus most likely resulted in a high accumulation of strain and thus an elevated level of seismic hazard.

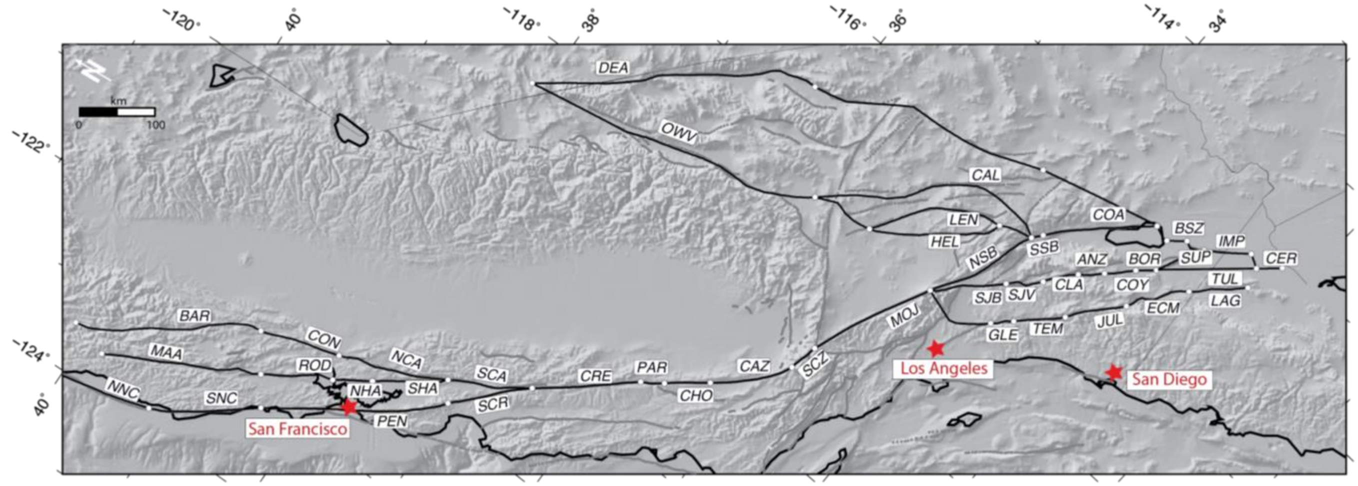

Figure 1. San Andreas Fault System segment map. Topography map of California with black lines representing the major fault segments of this study. The fault segment labels correspond to model details provided in Appendix A.

While the volatile nature of the SAFS has resulted in it being one of the most heavily studied fault systems on Earth, there are still uncertainties surrounding its past and potential future behavior. To better characterize the SAFS and associated seismic risks, geodetic data provided by GPS, Interferometric Synthetic Aperture Radar (InSAR) and even tide gauges can be considered. Over the past decade the wealth of accumulated geodetic data has grown substantially in response to the NSF's EarthScope Initiative, and when successfully integrated, it is now possible to image the entire SAFS with unprecedented spatial coverage and resolution. The resulting surface velocity and deformation time series products provide critical boundary conditions needed for improving our understanding of how faults are loaded across a broad range of temporal and spatial scales. Specifically, the available geodetic data can be used, with the aid of realistic physical modeling tools, to determine physical properties of the Earth's crust, such as fault depths and slip rates, as well as rates of tectonic strain accumulation.

Working to utilize available geodetic data, horizontal velocity GPS observations and line-of-sight velocity InSAR data sets are analyzed for this study. The data sets were then used as velocity constraints to an existing 4D earthquake cycle model of the SAFS (Smith and Sandwell, 2004; Sandwell and Smith-Konter, 2018) to create a refined representation of time dependent earthquake cycle deformation processes. Significant modeling improvements were developed for this study, including a refinement of the existing model architecture to accommodate improvements in fault segment representation, variable crustal rigidity, and for future work, incorporating vertical velocity observations. The refinement of the SAFS model representation thus aims to advance the characterization of the seismic potential of the faults and their attributed seismic risk. This work will be further discussed in the following sections.

2 4D Earthquake Cycle Model

2.1 Model Construction

To quantify motions of the SAFS, I use a physics-based model of 3D motions on connected fault planes that simulate earthquake cycle strain accumulation in the upper brittle crust, and viscoelastic relaxation in the lower crust and upper mantle. The elastic/viscoelastic deformation modeling code, Maxwell (developed by Smith and Sandwell (2004)) is used for this study. Maxwell uses a semi-analytical Fourier domain approach to rapidly compute 4D deformation across a high-resolution grid, thus making it possible to simulate high-resolution (1km) horizontal and vertical motions of the earthquake cycle of the SAFS over 1000-year time scales. This computationally efficient model is advantageous over complimentary methods as it is capable of computing multiple time steps spanning a spatial domain of several thousand kilometers in under two hours using a single core. This efficiency permits detailed analysis of how variable slip rates, locking depths and crustal rigidity work together to slowly accumulate strain, episodically generate significant earthquakes, and subtly respond to stress relaxation. Additionally, the model can be used to reproduce past recorded motion to verify its reliably for future estimates.

To accurately represent the SAFS, the model is comprised of 46 major fault segments within an elastic layer, overlying a viscoelastic half space. Each fault segment is assumed to be vertical strike-slip (90-degree dip angle) and extends from the surface to an assigned (or solved for) locking depth (Figure 2). Secular slip is prescribed from the base of the locked zone to the base of the elastic plate while episodic shallow slip is prescribed form the surface to the locking depth based on historical earthquake records and geologic recurrence intervals. Three components of velocity or displacement (i.e., horizontal Vx, Vy, and vertical Vz) are computed for each fault segment as a function of depth (Figure 3). A majority of the values adopted for the segments of this study come from previous collaborative work reported in Tong et al. (2014). The specific segment parameters are described in Appendix A. The crust and mantle of the model is additionally defined by parameters pertaining to the surrounding geologic setting of the faults such as material density, viscosity, shear modulus and elastic plate thickness. The complete model architecture is described in Figure 2.

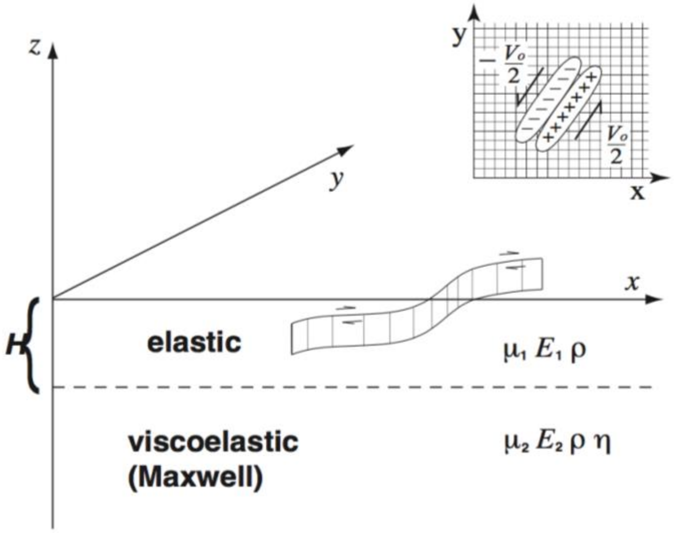

Figure 2. Image adopted from Smith and Sandwell (2004) of the viscoelastic deformation modeling code, Maxwell. The model is characterized by an elastic layer, with thickness H, above a viscoelastic half space. The elastic layer is allocated a shear modulus, Young’s modulus and density, while the viscoelastic half-space is additionally assigned a value of viscosity. Fault segments are prescribed a locking depth, slip rate, recurrence interval and earthquake history.

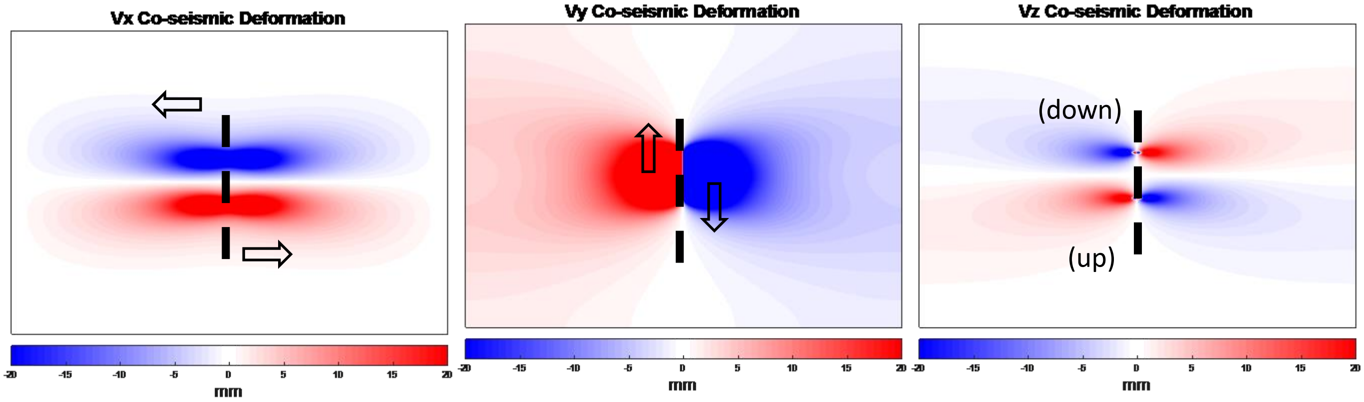

Figure 3. Map view of example 3D coseismic deformation output from the Maxwell modeling code for horizontal (Vx and Vy) and vertical (Vz) velocities from a strike-slip fault. For this example, 2m of strike-slip is prescribed along a fault that extends from the surface to 10km depth.

2.2 New Model Developments (Variable Crustal Rigidity)

Sandwell and Smith-Konter (2018) recently added a new component of the Maxwell model (Maxwell_v) that permits specification of a spatially variable crustal rigidity, as opposed to a former homogeneous description. The model can now simulate a thicker or thinner elastic plate by implementing a variation in the assigned shear modulus (Appendix B). In the simplest of terms, a region with a thinner elastic plate will be reflected by a lower than average crustal rigidity. A lower crustal rigidity defines the crust as less rigid and easier to deform. The opposite occurs for regions with a thicker elastic layer, which will reflect an increased shear modulus and a higher crustal rigidity. The ability to further specify unique characteristics surrounding different fault segments, such as crustal rigidity, allows for a better representation of crustal dynamics of the SAFS.

2.3 Model Benchmarks

To test the implementation of the variable crustal rigidity parameter, simple 2D control models were developed to test the new model Maxwell_v against the standard (original) homogenous crustal rigidity computational code, Maxwell. The basic premise of these tests are to assess the changes in surface velocity surrounding a fault that encounters zones of low and/or high (with respect to some average) rigidity. For one test (Figure 4), a strike slip fault (comprised of 13 segments) along the center of the model space was established, where the segments intersect the center of a square region of prescribed low rigidity (15 GPa) followed by a region of average rigidity (30 GPa), and then a high rigidity (45 GPa). The two units of extreme rigidity are separated by a distance of 200km in the y-direction. A 30 GPa background crustal rigidity (the geologic average for this region) was also used for this test model. All segments were assigned a slip rate of 40mm/yr extending from the surface to 10km depth, where segments 1,2,6,7,8,12 and 13 lay completely in the average rigidity region, while the lower segments (3-5) are placed within the low rigidity unit and the higher segments (9-11) are placed within the high rigidity unit. For all the segments, lengths do not straddle rigidity boundaries and thus lay completely within one rigidity region.

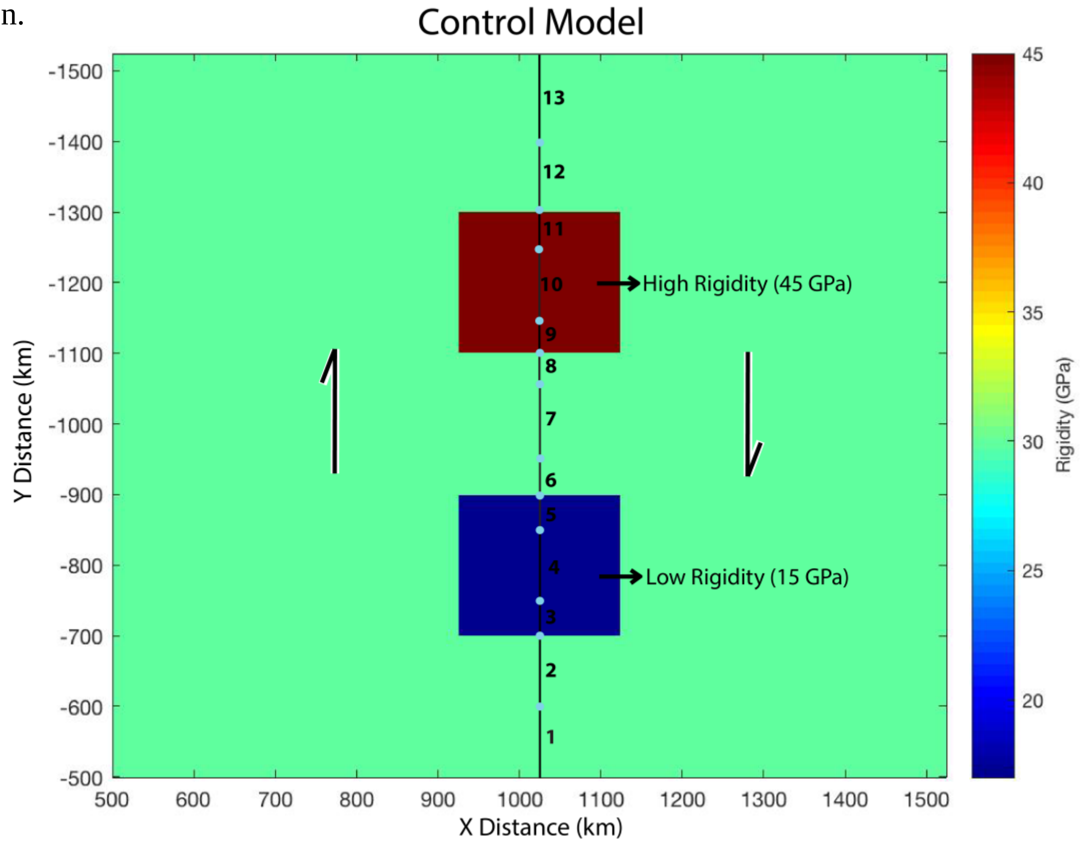

Figure 4. Example benchmark model set up for the variable crustal rigidity (Maxwell_v) model. The control model for the homogeneous crustal rigidity (Maxwell) model contains a homogenous rigidity grid of the average 30 GPa rigidity.

A forward Maxwell (homogeneous crustal rigidity) model was first run which implemented standard crustal rigidity of 30 GPa, followed by a forward Maxwell_v (variable crustal rigidity) model. The goal here was to assess the changes seen in deformation between the two models. These results are compared in Figure 5, where interseismic motion for the strike-slip fault system within a homogeneous crustal rigidity model (Figure 5A left) resulted in a consistent surface velocity across the fault boundary, with 20mm/yr partitioned symmetrically across the velocity arctangent function (Weertman and Weertman, 1966). When introducing the same fault system to regions of 50% lower and higher rigidity in the variable crustal rigidity model (Figure 5A right), the resulting surface velocity varied throughout the regions. Velocity residual maps (variable – homogeneous crustal rigidity) are also provided for the three difference components of the velocity field (Figure 5B). These results show that for regions within a higher rigidity, the expected simple motions in Vx, Vy, and Vz (seen in Figure 3) decrease in deformation rate and the opposite motion deformation occurs. This result must then correspond to a lessened motion from the variable rigidity model compared to the motion from the homogenous model. Alternatively, regions with lower rigidity display an increased expected motion deformation rate, meaning more deformation must have occurred in the variable model compared to the homogenous model. Several other test cases reflecting variations in locking depths of the segments, elastic thickness and viscosity were also considered (Table 1); regions of lower than average crustal rigidity had increased rates of deformation by at least 66% and in contrast, regions of higher than average crustal rigidity had decreased deformation rates by at least 61%. These results support the expectation that a lower crustal rigidity, simulating a less rigid elastic plate, will be easier to deform, while a higher crustal rigidity subsequently results in a more rigid and more difficult to deform plate.

Horizontal Vy Deformation for Variable Crustal Rigidity Control Models (mm/yr)							
Grid Position (x,y), assigned rigidity	Parameters: A	B	C	D	E	F	G
(1020,1200), 45 GPa	2.64	4.82	1.77	2.39	2.69	2.64	2.64
(1020,1000), 30 GPa	4.19	7.63	2.79	3.87	4.25	4.19	4.19
(1020,800), 15 GPa	7.25	12.69	4.86	6.79	7.32	7.25	7.25

Table 1. Results for interseismic variable crustal rigidity control models depicting horizontal Vy deformation in mm/yr. Parameters for A are determined by a 10km fault locking depth, a 60km thick elastic layer and a viscosity of 1e19Pas. The A parameters represent the control model for this study. The remaining parameters deviate from the control by the following; B assumes a shallower

locking depth of 5km, C assumes a deeper locking depth of 15km, D assumes a thinner elastic plate of 30km, E assumes a thicker elastic plate of 90km, F assumes a less viscous viscoelastic layer of 1e18 Pas and G assumes a more viscous viscoelastic layer of 1e20 Pas (which are presented here for completeness, as the viscosity has no effect on velocity variations for the interseismic model reflected here).

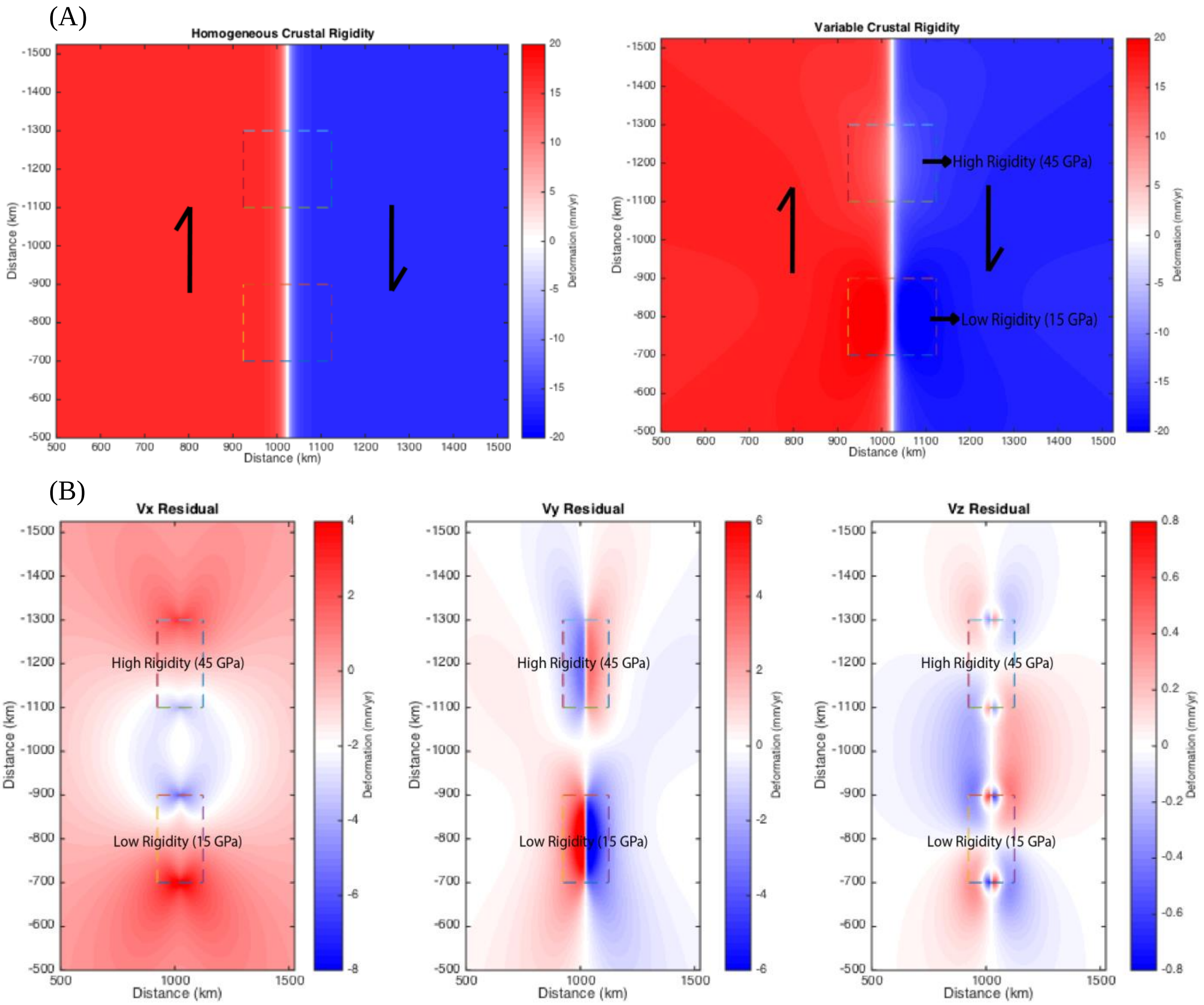

Figure 5. Benchmark of the effect of variable crustal rigidity for an interseismic velocity model of the earthquake cycle. Both homogeneous and variable crustal rigidity models consider

parameters A (see Table 1): fault locking depth = 10km, elastic layer thickness = 60km, viscosity of viscoelastic layer = 1e19Pas. (A) Maxwell and Maxwell_v Vy (horizontal, fault-parallel component) grid. (B) Residual velocities (Maxwell_v – Maxwell) grids in the x, y and z-directions.

2.4 Model Inversion for Fault Slip Rates

The models utilized in this study are uniquely scripted for the ability to invert for some model parameters, such as locking depths and slip rates of faults, using available geodetic data. This feature allows models to be constrained by robust and updated surface deformation observations of the SAFS from GPS and InSAR velocities. The model inversion is explained at length in Tong et al. (2014) and the system of linear equations used for the inversion are as follows.

$$\bar{\bar{G}}\bar{m} = \bar{d} = \begin{bmatrix} \overline{\overline{G_g}} & \overline{\overline{E_g}} & \bar{\bar{I}} & \bar{\bar{r}} \\ \bar{\bar{G}}_\iota & \bar{\bar{E}}_\iota & \bar{\bar{I}} & \bar{\bar{r}} \\ \bar{\bar{C}} & 0 & 0 & 0 \\ 0 & \bar{\bar{S}} & 0 & 0 \end{bmatrix} \begin{bmatrix} \bar{s} \\ \bar{p} \\ \overline{v_0} \\ \overline{w} \end{bmatrix} = \begin{bmatrix} \overline{v_g} \\ \bar{I} \\ \overline{S_c} \\ 0 \end{bmatrix}, \quad \overline{\overline{[G^T}}\bar{\bar{G}}]^{-1}\overline{\overline{G^T}}\bar{d} = \bar{m} \qquad (2)$$

The parameters within the first matrix, $\bar{\bar{G}}$, of Equation (2) are the Green's functions for modeled surface velocity corresponding to $\overline{\overline{G_{g,\iota}}}$ and $\overline{\overline{E_{g,\iota}}}$, (subscripts g and i relate to GPS and InSAR observation locations respectively). The modeled velocity of $\bar{\bar{G}}$ is determined from the earthquake cycle model described in Section 2.1 and the modeled velocity of $\bar{\bar{E}}$ relates to a dislocation model reliant on the elastic parameters of the material (Tong et al., 2014). $\bar{\bar{I}}$ is the identity matrix, $\bar{\bar{r}}$ is the location of the velocity measurements with respect to the rotation axis, $\bar{\bar{C}}$ is the constraint matrix, and $\bar{\bar{S}}$ is the smoothing matrix. The vector $\bar{m}$ contains the parameter that is being solved for, such as slip rate, $\bar{s}$. It also contains values pertaining to creep rates, $\bar{p}$, and translation and rotation terms $\overline{v_o}$ and $\bar{w}$. The data observations are contained in vector $\bar{d}$, where $\overline{v_g}$ represents GPS vector velocity measurements, $\bar{I}$ represents InSAR line-of-sight velocity measurements and $\overline{s_c}$ represents types of geologic constraints: apriori estimates of slip rate from geologic data or the sum of slip rates on subparallel faults must equal the total slip rate across the plate boundary (45 mm/yr for the SAFS).

To demonstrate the utility of this method, the example control models of Section 2.3 were inverted for the best fitting slip rates for each fault segment. For this, 'synthetic' GPS and InSAR data were created based on the homogenous rigidity grid in Figure 5A to imitate observed real world geodetic velocities on the Earth's surface. The inversion code was then implemented to generate Green's functions for surface velocity and solves for the set of slip rates that minimizes the misfit between the synthetic data and model. The inversion results for the homogenous crustal rigidity model assigned each segment a ~40mm/yr slip rate (Figure 6A), which is to be expected as each segment was subjected to the same crustal rigidity and was assigned an initial slip rate which matched the synthetic data observations.

The results for the variable crustal rigidity control model inversion are displayed in Figure 6B. As expected, the inversion result for segment 4, which was solely subjected to a region of lower crustal rigidity and not at any boundaries, was much lower (24.47mm/yr) than the prescribed rate (40mm/yr). This can be explained by the previously discussed Maxwell_v results of a higher deformation rate for the region of lower crustal rigidity, and more importantly, a higher rate than the synthetic data rates that were used to constrain the model through the inversion. Recall that the synthetic data reflected slip rates congruent with a homogeneous crustal rigidity model where each fault slipped at a constant 40mm/yr (Figure 5A). Using these constraints, the inversion forces the slip rates to decrease in regions of higher effective deformation rates (like a reduced rigidity) in order to approximate the deformation observed by the synthetic data. In contrast, the inversion result for segment 10, which was solely subjected to a region of higher crustal rigidity and not at any boundaries, was much higher (49.18mm/yr) than the prescribed 40mm/yr rate. The model's deformation rate estimation for the region of higher crustal rigidity was much lower than average. Thus, the inversion result for effective slip rate must be much greater than the prescribed rate to reproduce a grid similar to the observed deformation from the synthetic data since the area is more rigid and more difficult to deform.

Segments 3 and 5, which were in the low rigidity region and at boundaries, still favored the low rigidity regions as the inversion assigned effective slip rates that were under the prescribed 40mm/yr. Segments 9 and 11, which were in the high rigidity region and at boundaries, preferred the high rigidity region as the inversion assigned effective slip rates over 40mm/yr. Segments 2, 6, 8 and 12, which were within the average rigidity region but at the boundaries, favored the extreme rigidity assigned to the region across the boundary. The inversion assigned a slightly lower effective slip rate to segments 2 and 6 and a slightly higher effective slip rate to segments 8 and 12. Lastly, segments 1, 7 and 13, which were completely in the average rigidity region and at no boundaries seems to experience little alteration from the variable rigidity grid as the inversion assigned effective slip rates very close to 40mm/yr.

A

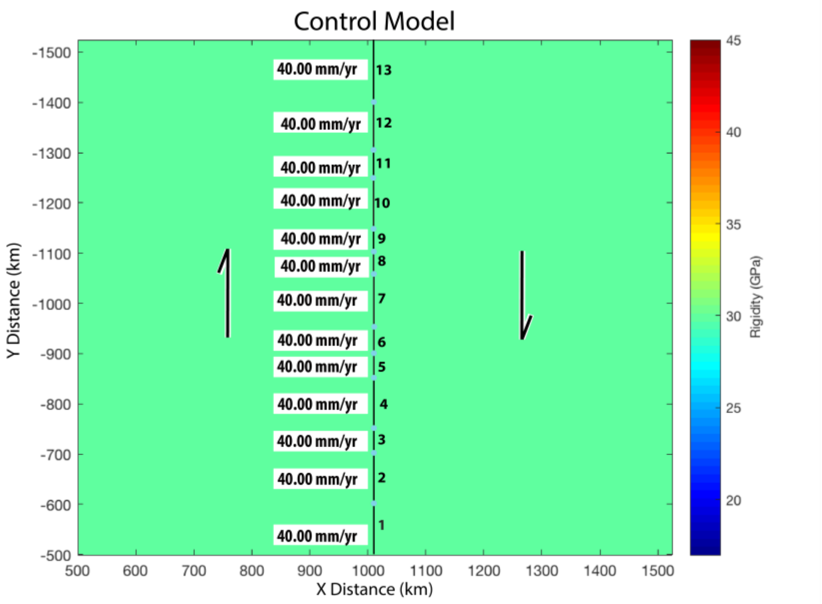

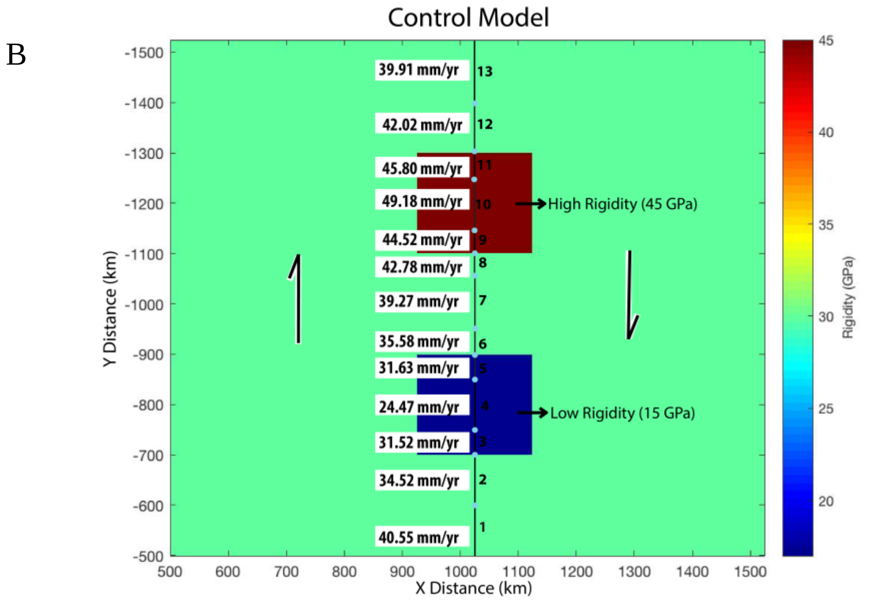

Figure 6. Benchmark inversion results of fault segment slip rates for (A) a homogeneous rigidity model and (B) a variable rigidity model. Synthetic data representing an ensemble plate boundary with a 40mm/yr slip rate were used in this inversion. Inversion results for slip rate are labeled next to each fault segment.

3 Data

3.1 Geodetic Observations

To constrain interseismic deformation of the SAFS, two GPS data sets and two InSAR data sets were considered. One GPS data set (largely UCERF-3, Tong et al. (2014)) includes 1981 horizontal velocity observations and is used as a reference data set to check reproducibility of results. The second GPS data set (adopted from the SCEC CGM) includes 2149 horizontal velocity observations (Crowell et al., 2013; McCaffrey et al., 2013; Herring et al., 2016; Zeng et al., 2016). Both GPS data sets' horizontal velocity vectors were projected into the SAFS model Cartesian space before analysis (Sandwell and Smith-Konter, 2018). The two GPS data sets are displayed in Figure 7A.

To further validate and compliment the capability of GPS observations, InSAR line-of-sight (LOS) velocity observations were additionally considered. InSAR observations were provided from the ALOS satellite (2006-2011) containing 53792 ascending LOS velocity observations (Figure 7B). Sentinel-1A (2014-2016) descending data (53507 LOS velocity observations) were also used in this study (Figure 7C). As with the GPS data, LOS velocity vectors were projected into the SAFS model Cartesian space before analysis.

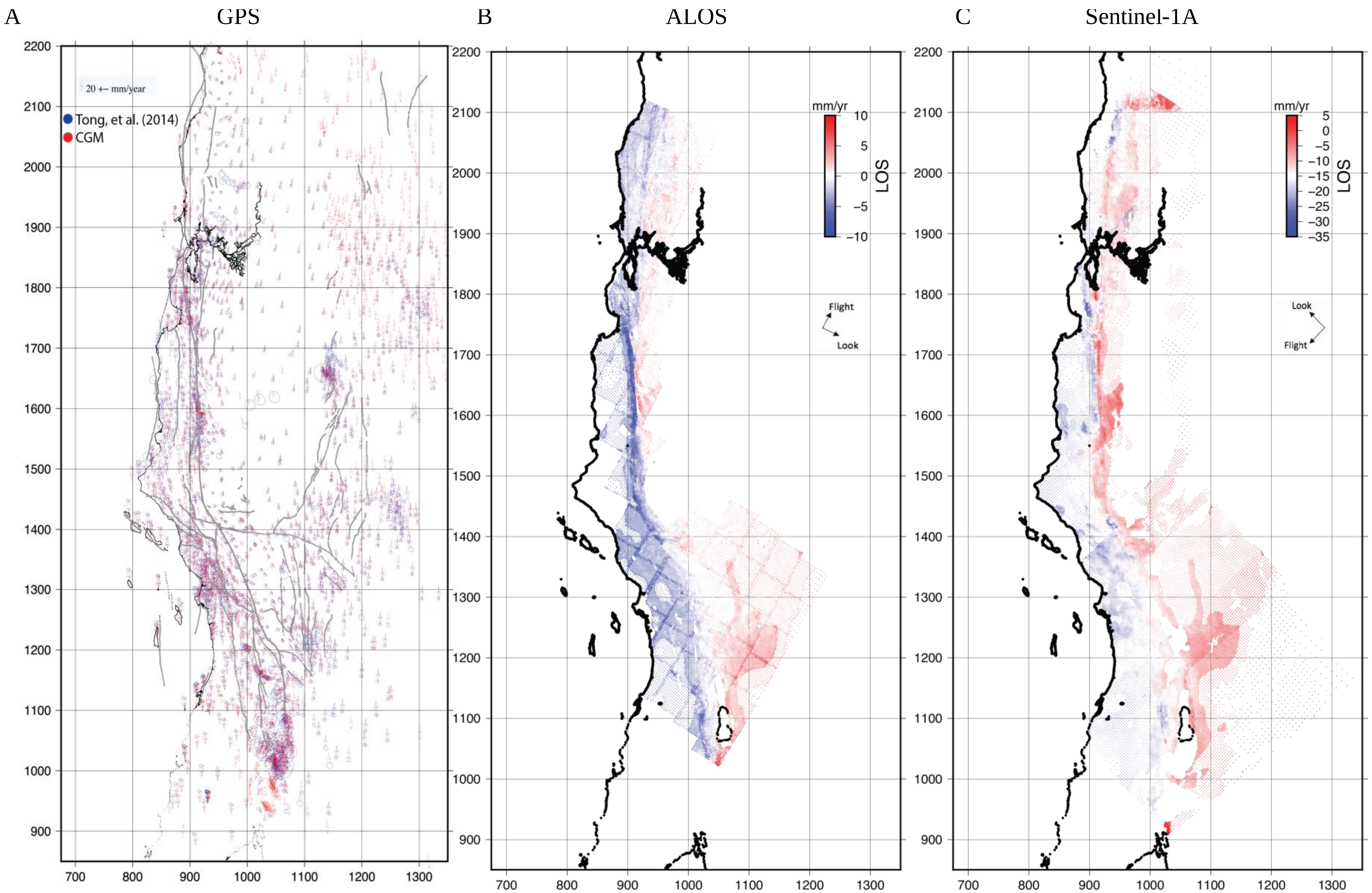

Figure 7. Geodetic data considered for this study. (A) GPS horizontal velocity vectors and uncertainties. Blue vectors depict the Tong et al. (2014) data set. Red vectors represent the SCEC CGM data set. (B) ALOS InSAR LOS velocity data. (C) Sentinel-1A InSAR LOS velocity data. For both B and C, positive (red) velocities represent ground motion away from the satellite and the flight path and look direction are delineated with labeled arrows.

3.2 Constructing a Model of Variable Crustal Rigidity of the SAFS

The final contribution of data to this study is that used to define reasonable crustal rigidity variations along the SAFS plate boundary. A basic crustal rigidity grid for California was developed based on seismogenic depths to the lithosphere-asthenosphere boundary (LAB) (Lekic et al., 2011) and surface heat flow data (Thatcher et al., 2017 (Figure 8)). The depth to the LAB is highly variable throughout California as different areas are subjected to regional tectonic settings. The Salton Trough for example, is subjected to extensional tectonic movement and to accommodate the extensional stain, the plate thickness of the region reduces (Lekic et al., 2011). The thinning of the plate results in a shallower LAB depth and subsequently greater surface heat flow. In contrast, the Sierra Nevada mountain range in northeast California produces a thickened region of the plate via an extended crustal root to maintain isostatic equilibrium within the Earth's crust to compensate for the substantial load from the mountains. The mountain range is also accepted as a region of lower surface heat flow. The relationship of depth to the LAB and surface heat flow was provided by the SCEC development of the Community Thermal Model (CTM) and is visually expressed in Figure 8 (Thatcher et al., 2017). A detailed description of how surface heat flow estimates are used to approximate changes in elastic plate thickness (through variation in the crustal rigidity parameter) is provided as supplementary material in Appendix B.

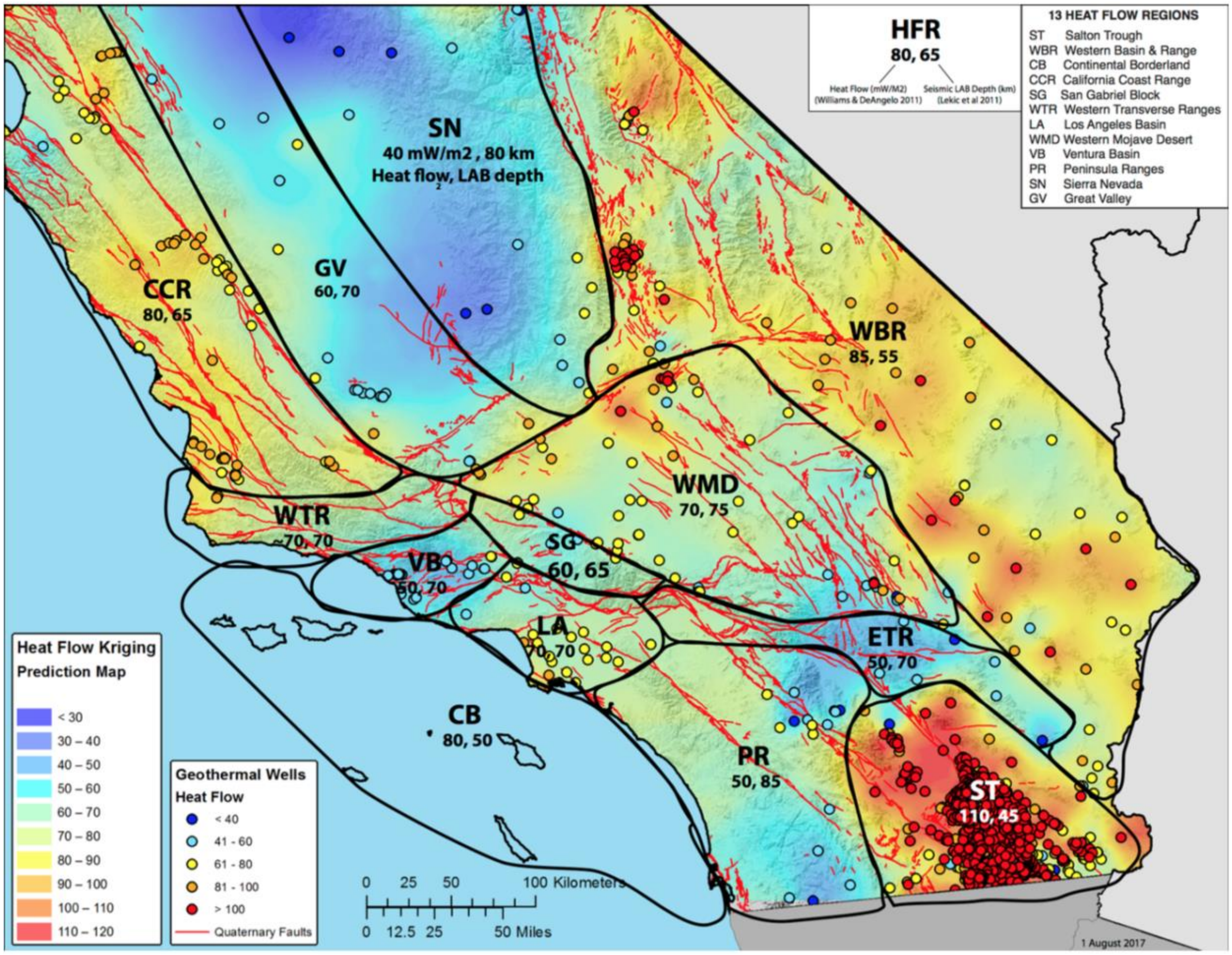

Figure 8. Surface heat flow and depth to the LAB for the greater portion of the state of California. Regions are defined and outlined in black (see legend upper right). Within each of the regions surface heat flow and depth to the LAB are assumed constant (figure from Thatcher et al., 2017).

4 Results & Discussions

4.1 Slip Rate Inversion Sensitivity Analysis

Following the simple inversion example in Section 2.4, a full inversion for slip rates of the SAFS segments was performed for both the homogenous and variable crustal rigidity models, and for all possible GPS and InSAR data set combinations. To investigate the sensitivity of the slip rate inversions, weights were first assessed for all combinations of GPS and InSAR data as well as the geologic slip rate constraints (C-matrix) inversions, and a weighted root mean square misfit (WRMS) (Equation 3) and χ^2 misfit (Equation 4) were calculated (Tong et al., 2014). The WRMS misfit considers the square root of the sum of the squared difference between the observation, o_i, and the model, m_i, normalized by the standard deviation of the observation, σ_i, and divides this by the sum of reciprocal of the standard deviation squared. The χ^2 misfit considers the squared sum of the difference of the observation and model normalized by the standard deviation of the observations, divided by the number of measurements, N.

$$WRMS = \sqrt{\frac{\sum_{i=1}^{N}(\frac{o_i - m_i}{\sigma_i})^2}{\sum_{i=1}^{N}\frac{1}{\sigma_i^2}}} \tag{3}$$

$$\chi^2 = \frac{1}{N}\sum_{i=1}^{N}(\frac{o_i - m_i}{\sigma_i})^2 \tag{4}$$

Four data/model combinations were run for this analysis, reflecting a range of weights that were considered for both the homogenous crustal rigidity model as well as the variable crustal rigidity model (Figure 9). The consistent optimal weights for all data set combinations were determined as a weight of 0.5 for the C-matrix, 0.3 for the InSAR data sets and 0.5 for the GPS data sets. Figure 9 also illustrates the sensitivity of various data combinations, when either InSAR data set was assigned a weight of over 1, the WRMS value for both GPS data sets began increasing dramatically. When either GPS data set was weighted 0.5 or higher, the GPS WRMS values became more stable and reflected little change. Additionally, when comparing the two InSAR WRMS values, Sentinel-1A consistently had values roughly double those of ALOS. Results of the best fitting models, utilizing these optimal weight combinations, are discussed in Section 4.2.

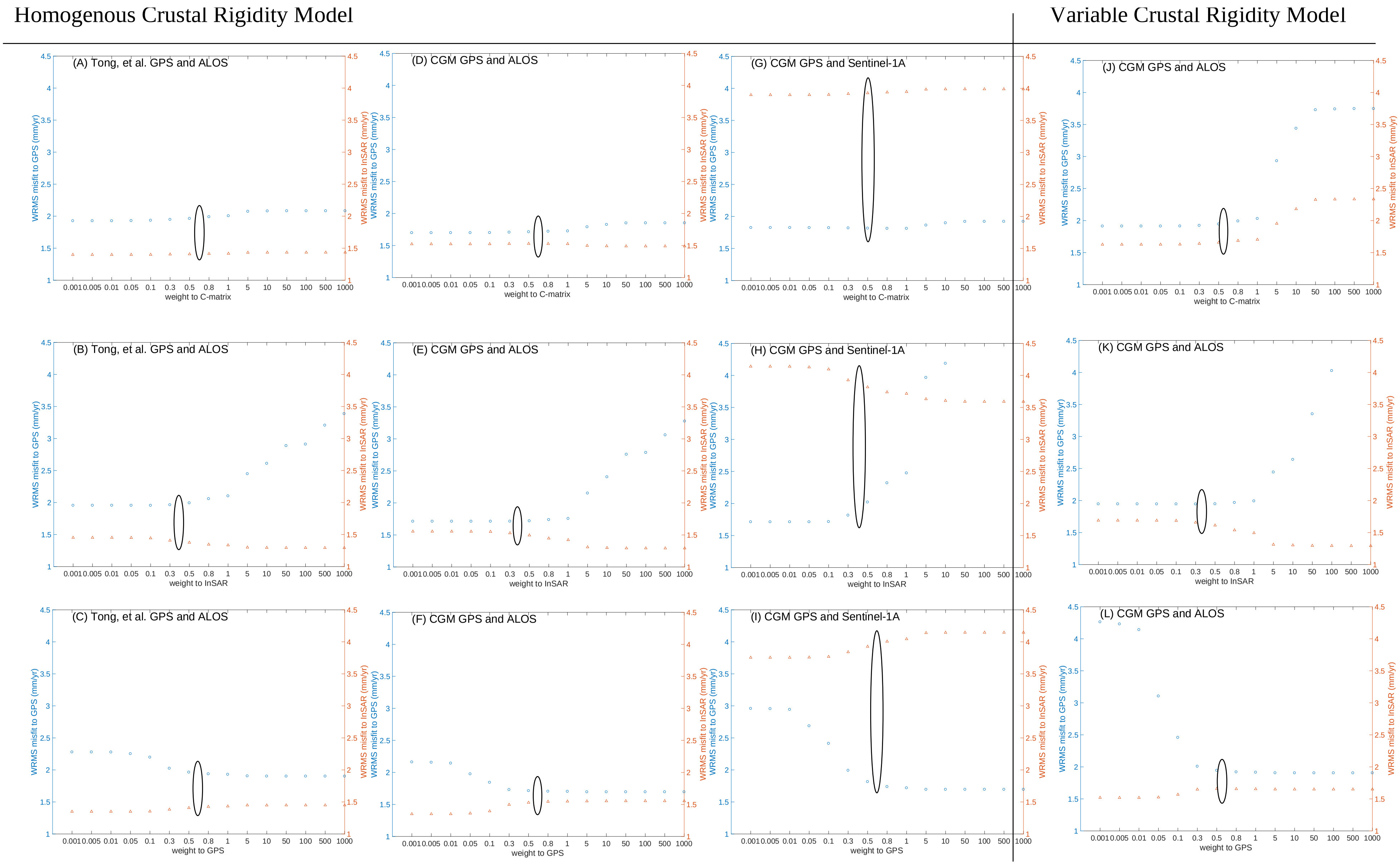

Figure 9. Slip rate inversion weights. Panels A-I display the range of weights considered for key homogeneous crustal rigidity model inversions for the three prescribed model constraints; the geologic constraints (C-matrix), InSAR data and GPS data. The consistent, optimal weights for all data set combinations were determined as a weight of 0.5 for the C-matrix, 0.3 for InSAR and 0.5 for GPS. The CGM GPS and ALOS InSAR combination, as seen in panels D-F, produce the smallest WRMS statistics and thus is the best fit to the earthquake cycle model. Panels J-L reflect the chosen CGM GPS and ALOS InSAR data set weight analysis for the variable crustal rigidity model.

4.2 Choosing an Optimal Dataset Combination

To understand the strengths (and weaknesses) of different geodetic data set combinations, forward models for both the homogenous and variable crustal rigidity models were also run for the SAFS. These models utilized a preferred slip rates from Tong et al. (2014) (Appendix A).

InSAR and GPS data set combinations				
Data Combination	WRMS misfit for GPS	WRMS misfit for InSAR	χ^2 misfit GPS	χ^2 misfit InSAR
Homogeneous Crustal Rigidity				
Tong et al. (2014) & ALOS	1.96	1.41	3.51	0.31
Tong et al. (2014) & Sentinel-1A	2.40	3.78	5.25	14.34
CGM & ALOS	1.71	1.53	20.62	0.37
CGM & Sentinel-1A	1.82	3.93	23.16	15.43
Variable Crustal Rigidity				
Tong et al. (2014) & ALOS	2.25	1.58	4.62	0.40
Tong et al. (2014) & Sentinel-1A	2.60	3.58	6.1545	12.84
CGM & ALOS	1.94	1.66	26.57	0.44
CGM & Sentinel-1A	2.01	3.70	28.43	13.74

Table 2. WRMS and χ^2 misfit values for each geodetic data set combination, reflecting weights of Section 4.1. These values reflect the goodness of fit between the earthquake cycle model and the geodetic observations and allows for the determination of the optimal data set combination. With 95% confidence, it was determined that the χ^2 misfit must fall below the critical value of 79.08 to be a good fit for our earthquake cycle model.

Considering the values of Table 2, while all data set combinations fell within the acceptable range of χ^2 misfit values, the earthquake cycle model produced the smallest WRMS misfit for the CGM GPS and ALOS InSAR velocity combination. The CGM GPS is the largest and most recent GPS data set considered with 2149 horizontal velocity observations, covering a sizeable range of the SAFS. The Tong et al. (2014) GPS data set, which was used as a reference, produced results that roughly matched their published misfit values and also provided a good fit between the model and data. However, when comparing the two GPS data sets, the newer CGM GPS compilation out preforms the Tong et al. (2014) GPS and was chosen. The Sentinel-1A data set contains the most recent InSAR observations when compared to ALOS, yet at this time, the ALOS data contained more observations and consistently provided a better fit for the models and thus was chosen for further analysis. The insufficient misfit results from the Sentinel-1A most likely comes from the absence of specific error observations at the time of analysis and thus every LOS velocity observation was assumed an error value of 1mm/yr. For future analysis when specific Sentinel-1A errors become available, it is expected to be the preferred InSAR data set.

4.3 New Interseismic Velocity Model Results

Using the inversion weights and optimal data combinations discussed in Sections 4.1 and 4.2, a final slip rate inversion was performed for both the homogenous crustal rigidity and variable crustal rigidity earthquake cycle models. These results and corresponding seismic moment accumulation rates (Equation 1) are provided in Appendix A. The resulting horizontal surface velocity grids (north-south and east-west velocity directions) are displayed in Figure 10. It is important to note that the slip rate inversion for the variable rigidity model yields *effective* slip rates based on the prescribed local crustal rigidity, which also has a (not-yet) quantified uncertainty. Comparing the deformation grid results for the homogenous and variable crustal rigidity models, it is clear that implementing variations in crustal rigidity has a regional impact on the SAFS earthquake cycle velocity model. Like the example model discussed in Section 2.3, a decrease in regional crustal rigidity (like that in the Salton Trough, southeast of San Diego) results in an increase in surface deformation rate. This increase in deformation rate occurs because the lower rigidity region is now easier to deform thus the model predicted deformation rate will be much faster than the deformation rate predicted for an average crustal rigidity region. As a result, in order to minimize misfit between the geodetic velocity observations and the modeled deformation, a slip rate inversion will solve for an *effective* lower slip rate for fault segments in the Salton Trough to better match the geodetic observations (this is consistent with the example model inversion results in Section 2.4).

East-West (Vx) Deformation

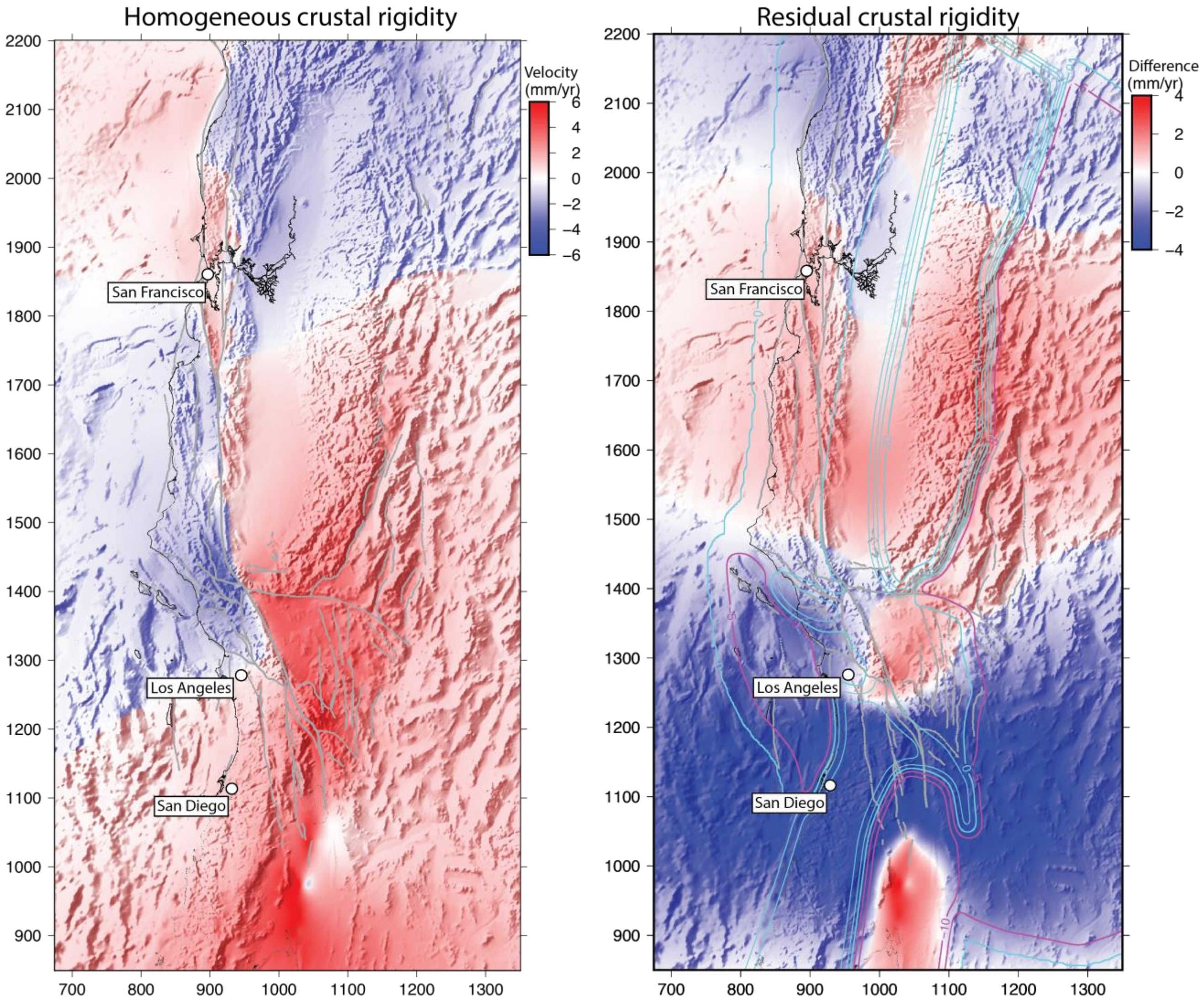

Homogeneous crustal rigidity

Residual crustal rigidity

North-South (Vy) Deformation

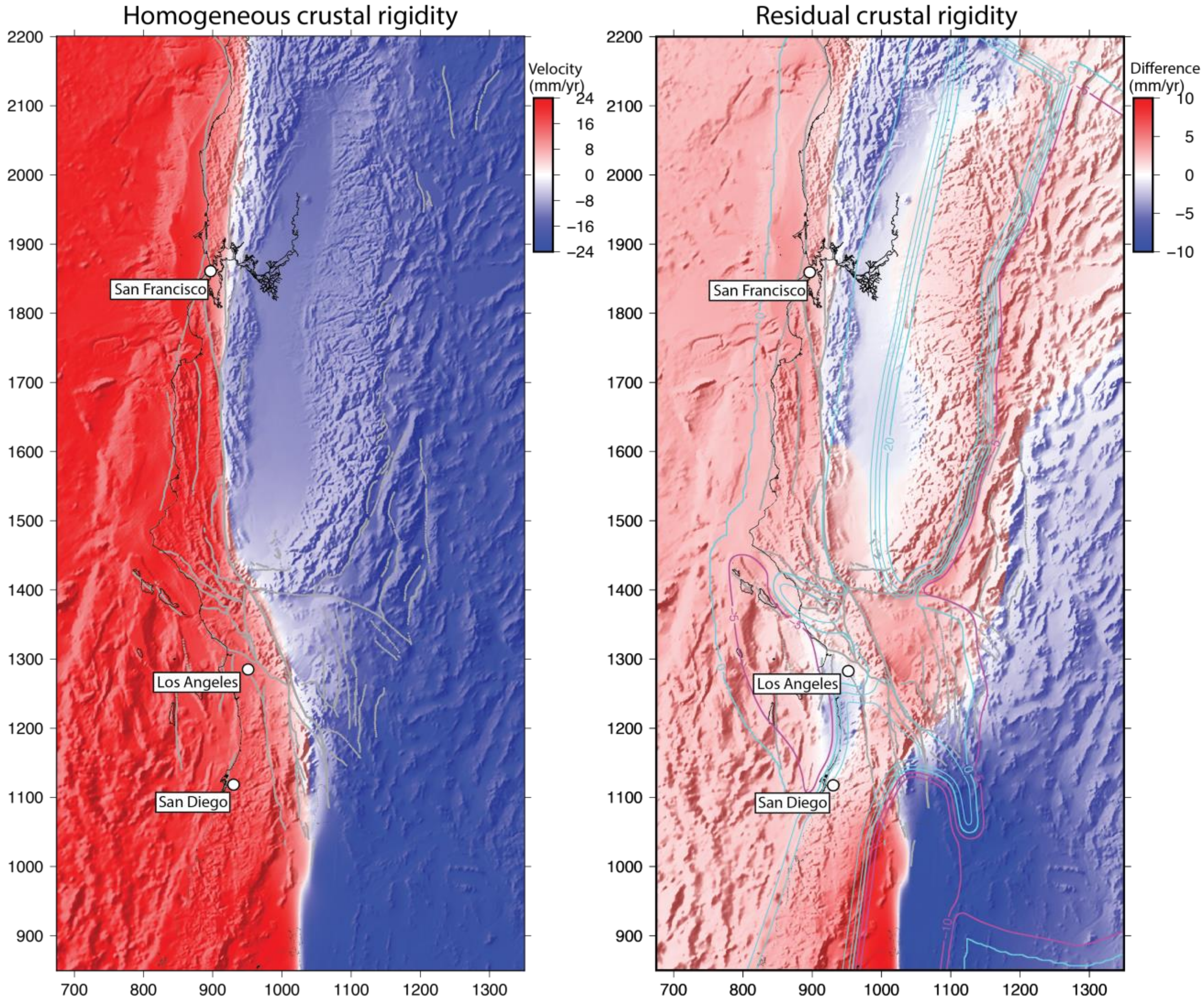

Figure 10. Horizontal components of surface earthquake cycle velocity (east-west (Vx) and north-south (Vy)) driven by deep slip and earthquake postseismic viscoelastic relaxation along the segments of the SAFS within a 60km thick elastic plate. Fault segment slip rates were determined by a model inversion with the optimal weighted geodetic data. Contours within the images represent rigidity deviation from the regional mean of 30 GPa; magenta is lower than average and cyan is higher than average. The east-west deformation images depict positive velocities (red) as eastward movement and negative velocities (blue) as westward movement. The north-south

deformation images depict positive velocities as northward movement while negative velocities represent southward movement. The residual images present the difference between the variable and homogeneous crustal rigidity model results.

5 Conclusion

To accurately interpret the variability of seismic potential of the SAFS, earthquake cycle models should both reflect realistic fault parameters and conform to optimal geodetic data constraints. The updated models in this study included improved model architecture, such as fault geometry, and for the variable crustal rigidity model, a realistic crustal rigidity representation for California. From this, two major conclusions resulted from this study: (1) Optimal geodetic velocity combinations for studying present-day motions are currently provided by CGM GPS and ALOS InSAR data sets, however as additional Sentinel data (with improved error analysis) become available, preferred use of Sentinel data over ALOS data is likely. (2) The effects of introducing variations in crustal rigidity (through manipulation of heat flow and LAB depth data) yield fairly significant changes in deformation rates for some segments of the SAFS; a decrease in regional crustal rigidity results in an increase in deformation rate, where the effective model slip rates (from inversion) decrease in response to the constraining geodetic surface deformation observations. Moreover, the significant changes that result when implementing a variable crustal rigidity model highlights the importance of incorporating characteristics specific to each fault segment to understand and replicate a more complete image of the SAFS. The evident differences between the homogenous and variable crustal rigidity model suggest that further seismic hazard quantification of the SAFS should consider the more inclusive variable crustal rigidity model.

Acknowledgments

I would like to thank my advisor, Dr. Bridget Smith-Konter, as well as my committee members, Dr. Paul Wessel and Dr. James Foster, for taking an interest in my research as well as me as a student. I would also like to thank Dr. Wayne Thatcher for providing the Southern California heat flow data.

References

Crowell, B. W., Y. Bock, D. T. Sandwell and Y. Fialko (2013), Geodetic investigation into the deformation of the Salton Trough, *J. Geophys. Res: Solid Earth*, 118, 5030–5039, doi:10.1002/jgrb.50347.

Field, E.H., G.P. Biasi, P. Bird, T.E. Dawson, K.R. Felzer, D.D. Jackson, K.M. Johnson, T.H. Jordan, C. Madden, A.J. Michael, K.R. Milner, M.T. Page, T. Parsons, P.M. Powers, B.E. Shaw, W.R. Thatcher, R.J. Weldon and Y. Zeng (2013), Uniform California earthquake rupture forecast, version 3 (UCERF3)—The time-independent model, *U.S. Geol. Surv. Open File Rep.,* 201*3–1165*, http://pubs.usgs.gov/of/2013/1165/.

Herring, T.A., T.I. Melbourne, M.H. Murray, M.A. Floyd, W.M. Szeliga, R.W. King, D.A. Phillips, C.M. Puskas, M. Santillan and L. Wang (2016), Plate Boundary Observatory and related networks: GPS data analysis methods and geodetic products, *Rev. Geo phys.*, 54, 59–808, doi:10.1002/2016RG000529.

Lekic, V., S. French and K. Fischer (2011), Lithospheric thinning beneath rifted regions of southern California, *Science*, doi:10.1126/science.1208898.

McCaffrey, R., P. Bird, J. Bormann, K.M. Haller, W.C. Hammond, W. Thatcher, R.E. Wells and Y. Zeng (2013), Appendix A-NSH-MP Block Model of Western United States Active Tectonics, Geodesy- and geology-based slip-rate models for the Western United States (excluding California) national seismic hazard maps, *U.S. Geol. Surv. Open File Rep.,* 2013–1293, doi:10.3133/ofr20131293.

Sandwell, D. and B. Smith-Konter (2018), Maxwell: A semi-analytic 4D code for earthquake cycle modeling of transform fault systems, *Computers & Geosciences*, 114, doi:10.1016/j.cageo.2018.01.009.

Smith, B. and D. Sandwell (2004), A three-dimensional semi-analytic viscoelastic model fortime-dependent analyses of the earthquake cycle. *J. Geophys. Res: Solid Earth*, 109, doi:10.1029/2004JB003185.

Smith, B. and D. Sandwell (2006), A model of the earthquake cycle along the San Andreas Fault System over the past 1000 years, *J. Geophys. Res.*, 111, doi:10.1029/2005JB003703.

Stein, R. S. (2007), Appendix D: Earthquake Rate Model 2 of the 2007 Working Group for California Earthquake Probabilities, Magnitude-Area Relationships, *U.S. Geol. Surv. Open File Rep.*, 2007-1162, http://pubs.usgs.gov/of/2007/1162/.

Thatcher, W.R., D.S. Chapman, A.A. Allam and C. Williams (2017), Refining Southern California geotherms using seismologic, geologic, and petrologic constraints. Poster Presentation at 2017 SCEC Annual Meeting.

Tong, X., B. Smith-Konter and D. T. Sandwell (2014), Is there a discrepancy between geological and geodetic slip rates along the San Andreas Fault System?, *J. Geophys. Res: Solid Earth*, 119, 2518–2538, doi:10.1002/2013JB010765.

Turcotte, D. L. and G. Schubert (2014), *Geodynamics*.

Weldon, R., T. Fumal and G. Biasi (2004), Wrightwood and the earthquake cycle: What a long recurrence record tells us about how faults work, *GSA Today*, 14, 4–10, doi:10.1130/1052-5173(2004) 014<4:WATECW>2.0.CO;2.

Weertman, J. and J.R. Weertman (1966), Elementary Dislocation Theory, *The Macmillian Company*.

Williams, M.L., K.M. Fischer, J.T. Freymueller, B. Tikoff, A.M. Tréhu and others, Unlocking the Secrets of the North American Continent: *An EarthScope Science Plan for 2010-2020*, February, 2010, 78p.

Zeng Y. and Z. Shen (2016), Appendix D—A Fault-Based Model for Crustal Deformation in the Western United States, Geodesy-and geology-based slip-rate models for the Western United States (excluding California) national seismic hazard maps, *U.S. Geol. Surv. Open File Rep.*, 2013–1293, doi:10.3133/ofr20131293.

Appendix A

Table A1. Earthquake cycle model parameters and seismic moment accumulation rate estimates for a homogeneous and variable crustal rigidity model. Segments impacted by a rigidity reduction, from the average 30 GPa, are shaded in gray.

Fault Label	Fault Name	Preferred Slip Rate (mm/yr)	Depth (km)	Moment rate per length (Nm yr^{-1} km^{-1}) x 10^{15}	Variable shear modulus (GPa)	Moment rate per length (Nm yr^{-1} km^{-1}) x 10^{15}
CER	Cerro Prieto	40.7	-5.1	3.9	17.5	0.8
CER	Cerro Prieto	40.1	-5.1	5.4	17.5	2.9
IMP	Imperial	44.0	-5.9	8.2	17.5	2.4
IMP	Imperial	19.7	-5.9	5.3	17.5	2.6
BSZ	Brawley	25.5	-15.3	16.5	17.5	1.9
BSZ	Brawley	25.7	-15.3	14.1	17.5	1.7
COA	Coachella	20.8	-11.5	7.8	27.02	5.0
SSB	South San Bernardino	23.3	-16.4	10.8	37.85	0.6
NSB	North San Bernardino	12.9	-17.8	7.3	34.19	12.0
SUP	Superstition Hills/ Mt	15.4	-10.8	2.4	17.5	0.1
BOR	Borrego Mountain	11.4	-6.4	2.2	17.55	0.1
COY	Coyote Creek	11.7	-8.0	3.3	20.29	4.4
ANZ	Anza	17.6	-4.5	2.1	32.87	2.9
CLA	Clark	10.1	-13.7	7.3	40.72	6.8
SJV	SJ Valley	14.4	-21.5	10.4	40.58	0.9
SJB	SJ San Bernardino Valley	6.3	-21	4.9	35.7	0.7
MOJ	Mojave	28.1	-16.8	14.6	30.46	18.1
SCZ	S Carrizo (Big Bend)	36.6	-11.5	11.1	30.67	14.2
CAZ	Carrizo	39.1	-11.5	13.5	30.47	10.0
CHO	Cholame	37.9	-9.1	10.7	29.87	8.4
PAR	Parkfield	14.9	-10.9	12.2	28.63	16.3
CRE	Creeping	23.0	-2.2	1.8	26.7	1.6
SCR	Santa Cruz Mt	10.6	-6.3	3.9	25.75	3.4
PEN	SA Peninsula	22.8	-16.2	10.6	25.75	3.2
SNC	S SA N Coast	23.9	-15.5	5.2	25.84	0.6
NNC	N SA N Coast	22.9	-13.2	8.4	25.77	0.1
SCA	S. Calaveras	23.9	-1.2	0.6	25.75	0.5
NCA	N. Calaveras	10.7	-0.3	0.1	25.78	0.1
CON	Concord	9.6	-0.8	0.2	26.02	0.1
BAR	H Creek/Bartlett Spring	9.0	-12	5.7	25.84	3.3
SHA	S. Hayward	9.4	-5.1	1.3	25.75	1.6
NHA	N. Hayward	9.8	-4.4	1.5	25.75	2.3

homogeneous rigidity model $\mu = 30$ GPa

variable rigidity model $\mu = 17\text{-}41$ GPa

ROD	Rodgers Creek	11.9	-4.5	homogeneous rigidity model	1.8	25.75	variable rigidity model	0.7
MAA	Maacama	10.9	-1.6		0.4	25.75		0.5
LAG	Laguna Salada	5.5	-9.0		0.3	17.54		0.2
GLE	Elsinore GlenIvy	4.4	-14.8		0.1	40.9		0.6
TEM	Elsinore Temecula	3.7	-14.8		0.2	41.0		6.8
JUL	Elsinore Julian	1.0	-14.8		0.3	40.81		0.6
ECM	Elsinore Coyote Mt	1.9	-14.8		0.4	26.88		0.4
CAL	Calico-Hildago	2.5	-15.0		0.5	33.17		0.5
LEN	Lenwood-Lockhart	5.4	-7.9		0.8	30.25		0.7
HEL	Helendale	1.2	-4.2		0.1	30.25		0.3
CAL	Calico-Hildago	9.1	-16.8		0.5	28.2		3.1
OWV	Owens Valley	6.5	-11.5		3.5	27.43		0.1
DEA	Death Valley	5.2	-1.5		0.1	22.5		0.1
TUL	Tulcheck	6.0	-10.0		0.3	17.5		0.2

Appendix B

To validate the connection between plate thickness and heat flow, the continental geotherm, as defined in Turcotte and Schubert (2014), is solved for the depth to the base of the elastic layer, z.

$$T(z) = T_o + \frac{q_m}{k} z + \frac{Q {h_r}^2}{k}\left(1 - e^{-z/h_r}\right) \tag{B1}$$

To interpret Equation (6) for California, the average surface temperature, T_o, is 10° C and the thermal conductivity, k, is $3.0 W m^{-1} C^{-1}$. q_m is the variable mantle heat flow, the surface radiogenic heat production, Q, is $2.5 \mu W m^{-3}$ and the effective thickness of the productive layer, h_r is $9 km$. The corresponding surface heat flow, q_o, for this model follows.

$$q_o = q_m + Q h_r = q_m + q_c \tag{B2}$$

For this model the variations in surface heat flow come from variations in mantle heat flow as the radiogenic heat generated in the upper crust, q_c, is assigned a constant value of $22.5 mW m^{-2}$. This results in a surface heat flow of $60 mW m^{-2}$ which relates to the average plate thickness of $60 km$. This average plate thickness is a value predetermined by Tong et al. (2014). Connecting to

Equation (6), the temperature at the base of the elastic layer was selected as $T_e = 800\,^\circ C$ to approximate the seismogenic depths to the LAB.

$$T_e(z_e) = T_o + \frac{(q_0 - q_c)}{k} z_e + T_c \tag{B3}$$

The temperature increase caused by the radiogenic layer, T_c, is $68\,^\circ C$. It is now possible to solve for the depth to the base of the elastic layer, z_e, for any given surface heat flow, q_o. Table 3 resolves the elastic thickness estimates for each of the regions in Figure 8.

$$Z_e = \frac{k(T_e - T_o - T_c)}{(q_o - q_c)} \tag{B4}$$

Heat flow Region	Heat flow (mWm^{-2})	Depth to $800\,^\circ C$ (km)	Depth to LAB (km)	Assigned model depth (km)
ST	110	25	45	35
WBR	85	35	55	45
CB	80	38	50	44
CCR	80	38	65	51.5
SG	60	58	65	61.5
WTR	70	46	70	58
LA	70	46	70	58
WMD	70	46	75	60.5
VB	50	79	70	74.5
PR	50	79	85	82.0
SN	40	124	80	102
GV	60	59	70	64.5
ETR	50	79	70	74.5

Table B1. Elastic heat flow estimates for the defined regions from Figure 8. The assigned model depths were the average of the depth to $800\,^\circ C$ determined by Equation (9) and the seismogenic depth to the LAB. The Salton Trough (ST) is a region of the plate that is significantly thinner with a thickness of only $35km$ compared to the average $60km$. In contrast to the ST, the Sierra Nevada (SN) region of the plate is much thicker than average at $102km$.

A subsequent elastic thickness for the regions in California (Figure 12) is thus produced based on the assigned model depth values calculated in Table 3. The scaled average shear modulus (30 GPa) by the average plate thickness ($60km$) is then multiplied by the elastic thickness of the region to produce an updated crustal rigidity via shear modulus. The map of Figure 8 is then digitized and turned into a grid to specify within the Maxwell_v code a given rigidity for specified region locations in the model space.

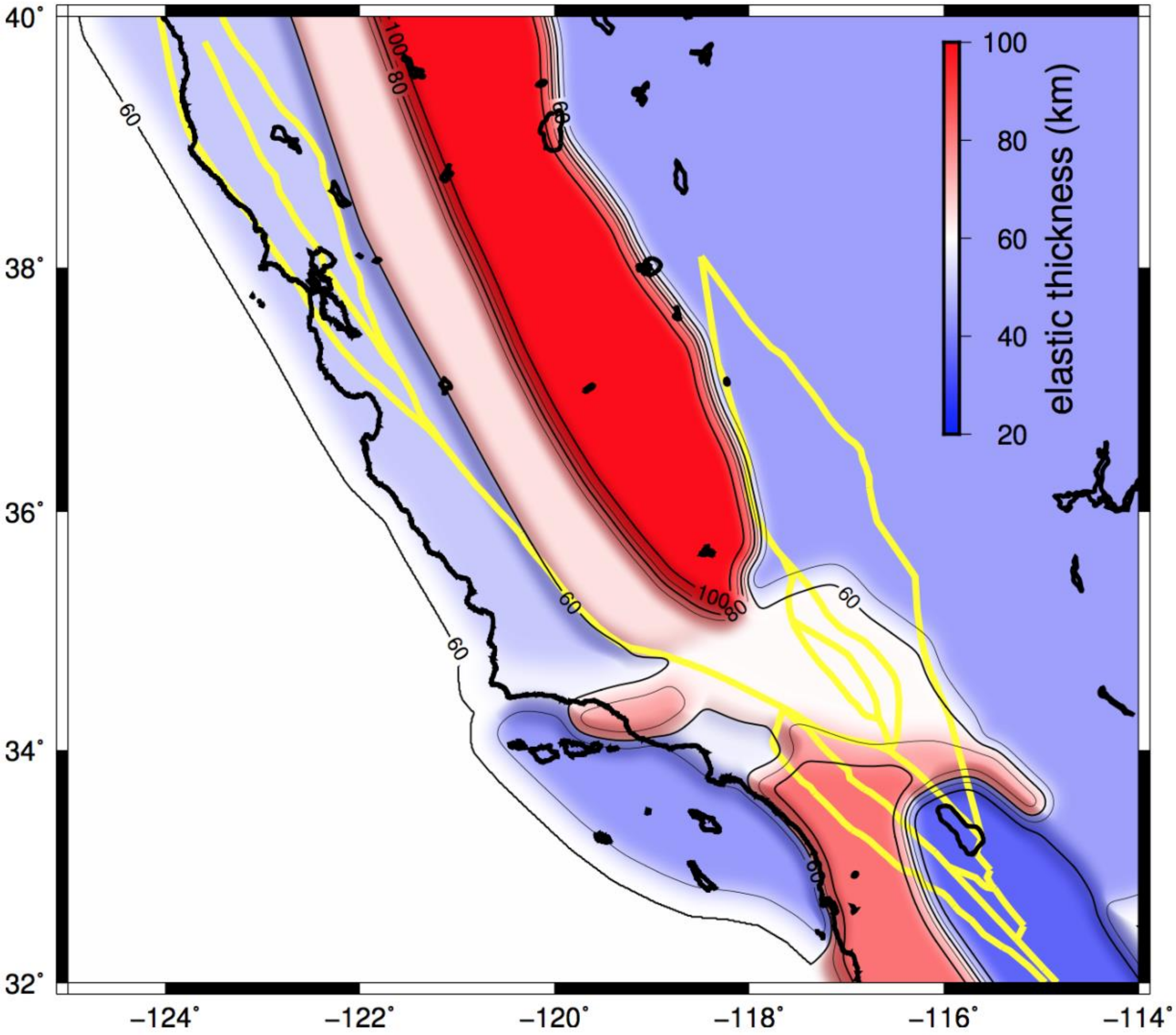

Figure B1. Map of elastic layer thickness throughout California. This figure was developed from previous work concerning surface heat flow and depth to the LAB provided by the SCEC CTM (Thatcher et al., 2017). The yellow lines represent fault segments used to delineate the SAFS in the Maxwell modeling code.